



Experimental and finite element simulation studies on hot deformation behaviour of AlCoCrFeNi_{2.1} eutectic high entropy alloy

M.R. Rahul ^a, Sumanta Samal ^{b,*}, S. Venugopal ^a, Gandham Phanikumar ^a

^a Department of Metallurgical and Materials Engineering, Indian Institute of Technology Madras, Chennai, 600036, Tamil Nadu, India

^b Discipline of Metallurgy Engineering and Materials Science, Indian Institute of Technology Indore, Simrol, Indore, 453552, Madhya Pradesh, India



ARTICLE INFO

Article history:

Received 12 January 2018

Received in revised form

19 March 2018

Accepted 21 March 2018

Available online 27 March 2018

Keywords:

Eutectic high entropy alloy

True stress-true strain curves

Processing map

Finite element simulation

Material flow behaviour

ABSTRACT

Hot deformation behaviour of AlCoCrFeNi_{2.1} eutectic high entropy alloy, consisting of fcc (CoCrFe-rich) and BCC (NiAl-rich) phases is studied by generating contour maps of multiple models using high temperature thermo-mechanical simulator compression test data. The workability regimes for thermo-mechanical processing are identified as 1073–1150 K and 10⁻³–10^{-2.2} s⁻¹ as well as 1338–1373 K and 10⁻³–10^{-1.2} s⁻¹. Finite element simulation has been used to study the strain distribution and material flow during hot deformation, which assists for predicting actual material flow in forging process. Flow instabilities during hot forming has been avoided by adopting integrated approach.

© 2018 Elsevier B.V. All rights reserved.

1. Introduction

The new alloy design concept of multicomponent high entropy alloys (HEAs) was first christened by Yeh et al. [1] and subsequently explored by many research groups in the last decade [2–8], owing to their excellent properties. The research work on HEAs has attracted significant attention due to its fundamental importance as well as practical implications. It is experimentally often observed that the multicomponent HEAs exhibit simple microstructure consisting solid solutions of FCC and/or BCC phases, which are attributed to the effect of alloying multiple elements in equiatomic or near equiatomic ratio. The simple structure in HEAs are the outcome of several core effects [9,10] such as high configurational entropy, severe lattice distortion and sluggish diffusion [11,12] which acts as a barrier for the formation of complex phases and also slow down the kinetics of phase transformations. Yeh et al. [1] reported the retention of strength up to 500 °C for the CuCoNiCrAl_xFe HEAs synthesized by casting and splat quenching. Senkov et al. [13] developed refractory HEAs such as Nb₂₅Mo₂₅Ta₂₅W₂₅ and V₂₀Nb₂₀Mo₂₀Ta₂₀W₂₀ alloys and observed the good mechanical properties at elevated temperature. The new class of

multicomponent eutectic HEAs (EHEAs) [4,6,14–16] have also been documented in the literature by different researchers; exhibiting good high temperature strength. Over the last few years, a lot of research work in the field of multicomponent HEAs has been carried out by many research groups to design new class of multicomponent HEAs by judicious selection of elements and composition to develop unique microstructural features so that the designed HEAs can be considered as potential candidates for possible structural and functional applications. Lu et al. [17] proposed the concept of EHEAs in AlCoCrFeNi_{2.1} alloy system, consisting of fcc and NiAl-phase, which was followed by many research groups [18–21] on the development of fully EHEAs by choosing elements and composition judiciously. Jiang et al. [18] designed and developed a series of fully eutectic microstructure in (CoCrFeNi)_M (M = Nb, Ta, Zr, Hf) alloy systems, namely, CoCrFeNiNb_{0.45}, CoCrFeNiTa_{0.4}, CoCrFeNiZr_{0.5} and CoCrFeNiHf_{0.4} EHEAs, consisting of FCC and Laves phases in the as-cast state. Jiang et al. [19] reported the fully eutectic microstructure in CoFeNiVMo_{0.6} (i.e. L → FCC + CoMo₂Ni) and CoFeNi_{1.4}VMo (i.e. L → FCC + Co₂Mo₃) alloy systems by systematically varying Mo and Ni concentration in CoFeNiVMo HEA. It is reported [20] in open literature that CoCrFeNi Nb_{0.45} EHEA consisting of FCC and Co₂Nb type Laves phase shows the good combination of compressive fracture strength of 2558 MPa and a fracture strain of 27.9%. Dong et al. [21] studied AlCrFeNiMo_{0.2} EHEA, comprised of AlNi-type intermetallic

* Corresponding author.

E-mail address: sumanta@iiti.ac.in (S. Samal).

compound and FeCr-type solid solution which exhibits excellent mechanical properties in terms of fracture strength of 3222 MPa and plastic strain of 0.287. Therefore, an attempt has been made in this direction to study the mechanical behaviour of new class of EHEAs, consisting of solid solution phase and intermetallic compound as a product of eutectics which can be used for high temperature structural applications. EHEA system has been chosen in the present investigation because of easy castability due to single melting point of the eutectic alloy as well as the possibility of achieving high strength due to lamellar morphology. It is also to be noted that eutectic alloys exhibit high strength due to Hall-Petch type relation [16] i.e. $\sigma_{ye} = \sigma_{0e} + k_H \lambda_e^{-1/2}$; where σ_{ye} is the yield strength of the material, σ_{0e} is the friction stress, k_H is Hall-Petch slope, and λ_e is the characteristic length in the eutectic i.e. known as interlamellar spacing. It is reported [22] that interlamellar spacing (λ_e) is directly related to diffusion coefficient (D) i.e. the value of λ_e decreases with low value of D. It is also mentioned in the open literature [12] that diffusion is sluggish in multicomponent high entropy alloys. Therefore, the EHEAs show high strength because of low value of the characteristics length (λ) of eutectic.

The present study of hot deformation behaviour and processing map of multicomponent AlCoCrFeNi_{2.1} EHEA was motivated by previous study pertaining to room temperature as well as high temperature mechanical properties of EHEA [17]. The objective of the present investigation is to identify the optimum thermo-mechanical processing (TMP) conditions of AlCoCrFeNi_{2.1} EHEA by generating contour maps using multiple parameters. The strain distribution and material flow behaviour during deformation has also been understood by using finite element method (FEM).

1.1. Experimental details

High purity commercial metals, namely Al, Co, Cr, Fe and Ni (>99.9%) were used as the starting materials. AlCoCrFeNi_{2.1} eutectic high entropy alloy (henceforth referred to as EHEA) was synthesized by arc melting under ultra-high purity argon gas on water cooled copper hearth to obtain arc melted alloy button. The arc melted alloy button was subsequently suction casting into a water-cooled split Cu-mold to obtain cylindrical rod having 6 mm diameter and aspect ratio of 13:1. The structural characterization of studied high entropy alloy was carried by X-ray diffraction (XRD) (Panalytical X-pert pro® instrument) with Cu-K α ($\lambda = 0.154056$ nm) radiation, operating at 45 kV and 30 mA, with step size of 20 = 0.017 deg. The peaks in the XRD pattern were identified using International Committee for Diffraction Data (ICDD) database in PCPDFWIN® software. The microstructural characterization of the samples was examined using the scanning electron microscope (Inspect F®) equipped with an energy-dispersive spectroscopy (EDS) and transmission electron microscope (TEM, FEI G²® with high-resolution capabilities). The thermal characterization of the HEA was carried out in argon atmosphere at heating rate of 20 °C/min. using differential scanning calorimetry (DSC) (Netzsch® STA 409). Isothermal hot compression tests of the cylindrical samples ($\phi = 6$ mm and aspect ratio of 1.5:1) were carried out using Gleeble 3800® thermo mechanical simulator at different deformation temperatures of 800 °C (1073 K), 900 °C (1173 K), 1000 °C (1273 K), 1050 °C (1323 K) and 1100 °C (1373 K) with constant strain rates of 0.001, 0.01, 0.1, 1 and 10 s⁻¹. A graphite sheet was kept at both ends of specimen and anvil along with Ni paste to ensure sufficient lubrication in order to avoid frictional effect during deformation. The cylindrical specimen was deformed to approximately 50% reduction in the height and was quenched with distilled water to freeze the microstructure at the testing temperature. The deformed specimen microstructural analysis was done along the compression

axis.

1.2. Simulation details

High temperature deformation process was simulated using commercial SIMUFACT® FEM software. Simulation process was carried out at different temperature and strain rate conditions. The average strain rate was achieved by controlling the stroke velocity and time for deformation. Simulation was carried out using quadrilateral element with size of 0.025 mm and assumed 2D-axisymmetric condition. Isothermal condition was used. Material mechanical properties are taken from the stress strain curves obtained from the flow stress test conducted at high temperature in Gleeble®. All other properties including thermal properties are calculated using rule of mixture criteria. Shear friction condition with an interface friction factor of 0.5 was used for frictional condition in between the die and the work piece. Material flow pattern with flow vectors is established. The strain field distribution inside the material during deformation is studied and correlated with the micro-hardness value.

2. Results and discussion

2.1. Structural characterization

The XRD pattern of multicomponent EHEA is shown in Fig. 1a. The XRD pattern shows the intense diffraction peaks corresponding to fcc solid solution phase (α) and intermetallic compound NiAl-phase.

2.2. Microstructural characterization

2.2.1. Scanning electron microscopic (SEM) observation

The detailed microstructural characterization of multicomponent EHEA was carried out using back scattered electron (BSE) imaging mode in SEM. However, the representative SEM micrograph of the studied EHEA is given in Fig. 1b to decipher the different phases in the microstructure. The different phases in the microstructure of the studied EHEA are marked based on the compositional analyses using EDS coupled with SEM. The microstructure of multicomponent EHEA reveals the presence of 100% eutectic microstructure at different length scale and is found to be consisting of CoCrFe-rich and intermetallic compound NiAl-rich phases.

2.2.2. Transmission electron microscopic (TEM) observation

The detailed TEM investigation of the studied multicomponent EHEA has been carried out to decipher the phases formed as well as the size and distribution of phases in the microstructure. However, the representative TEM micrographs of the studied EHEA is given here. The TEM bright field micrograph and corresponding selected area diffraction (SAD) pattern of the EHEA (shown in Fig. 2a) reveal the presence of eutectic microstructure at different length scale. It is clearly found that the phases in the microstructure are identified as BCC (NiAl-type) phase and FCC phase.

2.3. Thermal characterization

Differential scanning calorimetry (DSC) study was done in argon atmosphere in the temperature range of room temperature to 1500 °C at heating rate of 20 °C/min (Netzsch® STA 409). DSC curve (as shown in Fig. 2b) reveals the presence of one endothermic peak at 1362 °C, indicating the melting temperature of the studied multicomponent EHEA and also showing no other phase transformation in this temperature range.

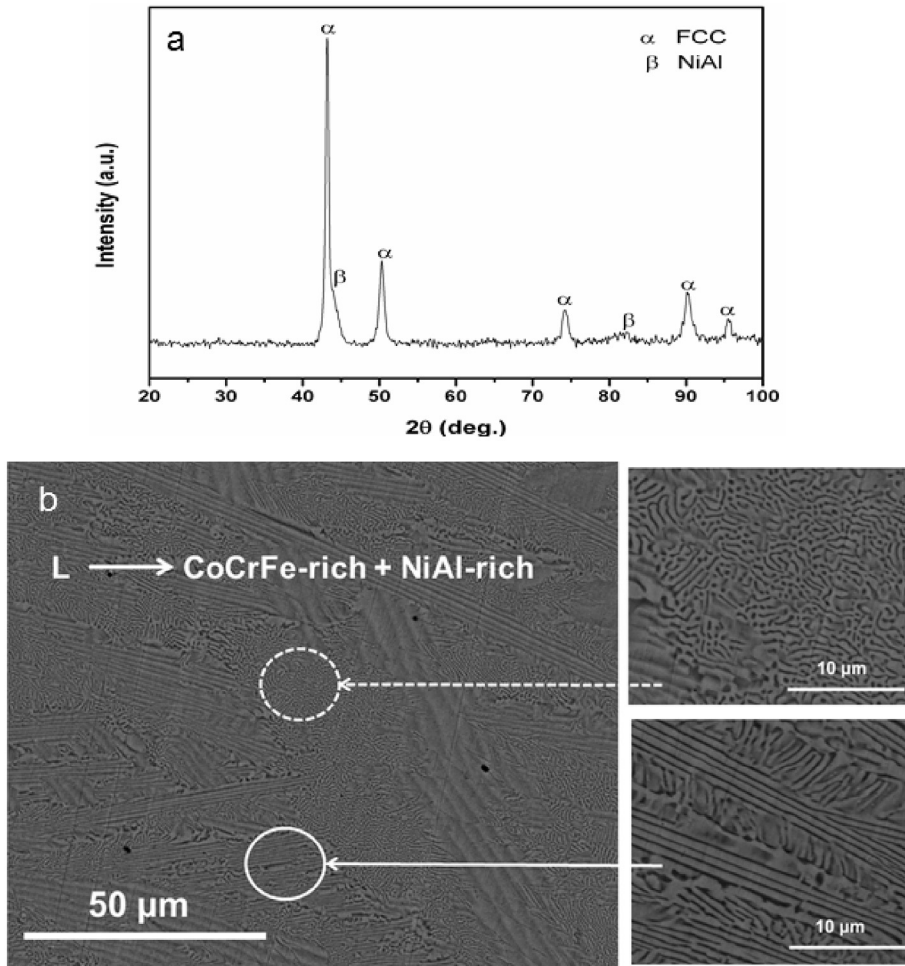


Fig. 1. (a) XRD pattern of as-cast AlCoCrFeNi_{2.1} EHEA and (b) BSE-SEM micrograph of as-cast AlCoCrFeNi_{2.1} EHEA.

3. Mechanical behaviour of multicomponent EHEA

The uniaxial true stress-strain curves of the multicomponent EHEA has been obtained for the suction cast cylinder with diameter (ϕ) = 6 with aspect ratio of 1.5:1 at different temperatures and at different strain rates.

3.1. Flow behaviour of EHEA

The uniaxial true stress-strain curves of the suction cast (ϕ = 6 mm and aspect ratio of 1.5:1) EHEA has been obtained at different temperatures 800 °C (1073 K), 900 °C (1173 K), 1000 °C (1273 K), 1050 °C (1323 K) and 1100 °C (1373 K) and different strain rates (i.e. 10^{-3} , 10^{-2} , 10^{-1} , 1 and 10 s^{-1}). The true stress (σ) – true strain (ε) plot of the EHEA obtained at different deformation temperature (T) and constant strain rate ($\dot{\varepsilon}$) is shown in Fig. 3. It is important to note that at a given strain rate ($\dot{\varepsilon}$), the flow stress of the material decreases with increase in temperature, whereas for a given temperature, the flow stress (σ) of material increases with increase in the strain rate which is consistent in all the observed test conditions. It is observed from Fig. 3 that the flow stress of the studied EHEA reaches the yield point, followed by softening. It has also been observed that the true stress and true strain curves are significantly influenced by the temperature and strain rate.

4. Modeling of flow curves: constitutive equations

The flow stress of a particular material (σ) is correlated with the strain (ε), strain rate ($\dot{\varepsilon}$) and temperature (T) by means of the constitutive equations. The constants in the constitutive equations are derived from the test data and validated with the experimentally determined values.

4.1. Determination of activation energy (Q)

The activation energy (Q) is the physical parameter, which signifies the plastic deformability. The Q-value can be calculated as follows.

The power law equation is given by

$$\dot{\varepsilon} = A_1 \sigma^n \exp\left[\frac{-Q}{RT}\right] \quad (1)$$

Taking logarithm of both sides of power law equation (1), we get

$$\log \dot{\varepsilon} = \log A + n \log \sigma - \frac{Q}{2.303RT} \quad (2)$$

After differentiating equation (2), we get

$$Q = 2.303R \left\{ \frac{\partial \log \dot{\varepsilon}}{\partial \log \sigma} \right\}_T \left\{ \frac{\partial \log \sigma}{\partial (1/T)} \right\}_{\dot{\varepsilon}} \quad (3)$$

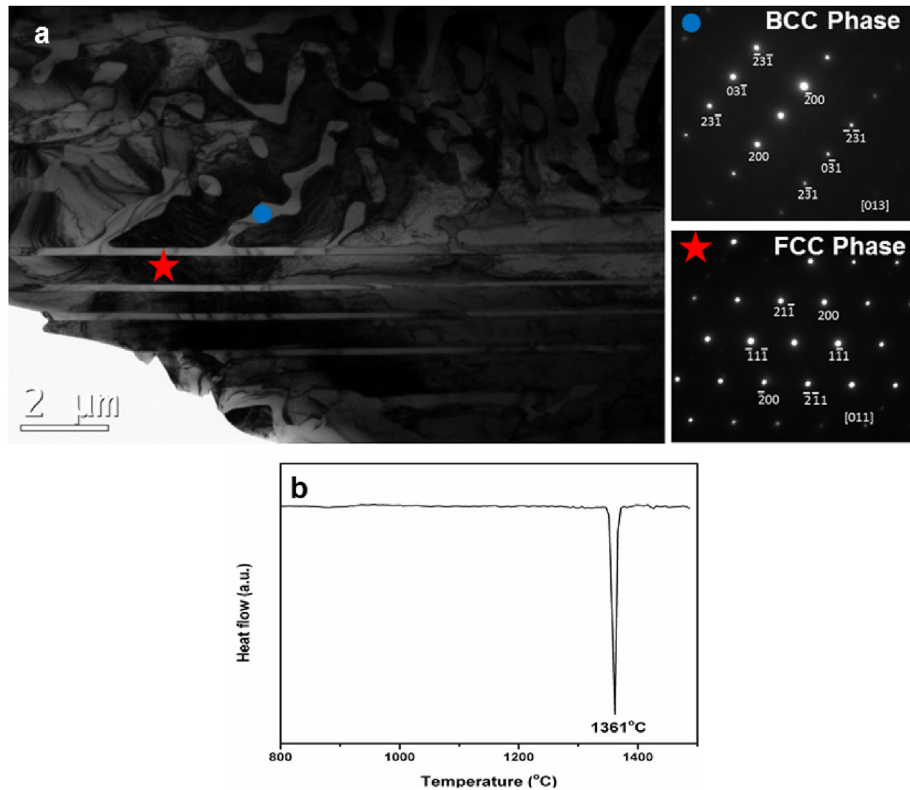


Fig. 2. (a) TEM micrograph of as-cast AlCoCrFeNi_{2.1} EHEA and (b) DSC plot of as-cast AlCoCrFeNi_{2.1} EHEA.

The first term $\frac{\partial \log \dot{\varepsilon}}{\partial \log \sigma}$ on the right side of equation (3) refers to the slope of $\log \dot{\varepsilon}$ vs $\log \sigma$ at different deformation temperature T, whereas the second term $\frac{\partial \log \sigma}{\partial (1/T)}$ refers to the slope of $\log \sigma$ and $1/T$ at different strain rate ($\dot{\varepsilon}$).

The activation energy (Q) for the multicomponent EHEA has been calculated at a strain of 0.6. The plot between $\log \dot{\varepsilon}$ and $\log \sigma$ at different deformation temperature T and $\log \sigma$ and $1/T$ at different strain rate ($\dot{\varepsilon}$) are shown in Fig. 4a and b respectively. It is found that the activation energy for the studied multicomponent EHEA is ~306 kJ/mol and the stress exponent value is ~5.6. Therefore, the constitutive equation which describes the flow stress of the multicomponent EHEA as a function of $\dot{\varepsilon}$ and T at strain (ε) of 0.6 can be written as:

$$\dot{\varepsilon} \sim \sigma^{5.6} \exp\left(\frac{306172}{RT}\right) \quad (4)$$

However, it is important to note that this constitutive equation for the studied EHEA describes the correlation between the strain rate and the stress within the temperature range 800–1100 °C. This activation energy is comparable to the commercial alloy such as Ti–6Al–4V consisting α -phase microstructure (i.e. Q ~265–370 kJ/mol) [23]. It is important to note that all elements in HEAs are assumed to be substitutional solutes and hence are thought to be one of the possible factor for the serrations in the flow curve of the present studied EHEA.

5. Generation of processing map

The processing map can provide information about the optimum deformation condition and to describe the flow instability domains. The investigated EHEA is subjected to plastic deformation

at different temperatures and strain rates to understand the deformation behaviour and develop processing map, a guide to thermomechanical processing. The deformation processing map for the EHEA has been generated using dynamic material modeling (DMM) which is applicable to the materials characterized by dynamic, nonlinear and irreversible phenomena [24–26] to understand the flow behaviour of the material under hot working conditions. The mechanical behaviour of the materials is characterized by the constitutive equations, which relate the flow stress (σ) to strain (ε), strain rate ($\dot{\varepsilon}$) and temperature (T). The DMM has been used to construct the processing maps i.e. superposition of the efficiency of power dissipation (η) and instability parameter $\xi(\dot{\varepsilon})$ of the investigated EHEA. This model assumes that the total instantaneous power absorbed by the work piece from the equipment is divided into two complimentary parts G and J which are given as; dissipater content G i.e. temperature rise because of the power dissipated through the plastic deformation and the dissipater content J is attributed to the microstructural change through various metallurgical processes. The total power absorbed P can be expressed as:

$$P = \sigma \dot{\varepsilon} = \int_0^{\dot{\varepsilon}} \sigma d\dot{\varepsilon} + \int_0^{\sigma} \dot{\varepsilon} d\sigma = G + J \quad (5)$$

The ratio $\frac{d\sigma}{d\dot{\varepsilon}}$ is equivalent to the strain rate sensitivity parameter (m) i.e. the ratio of the power attributed to metallurgical changes to the total plastic deformation. This is given by the following equation:

$$m = \frac{d\sigma}{d\dot{\varepsilon}} = \left(\frac{dJ}{dG} \right)_{T, \varepsilon} = \left(\frac{\partial \ln \sigma}{\partial \ln \dot{\varepsilon}} \right)_{T, \varepsilon} \quad (6)$$

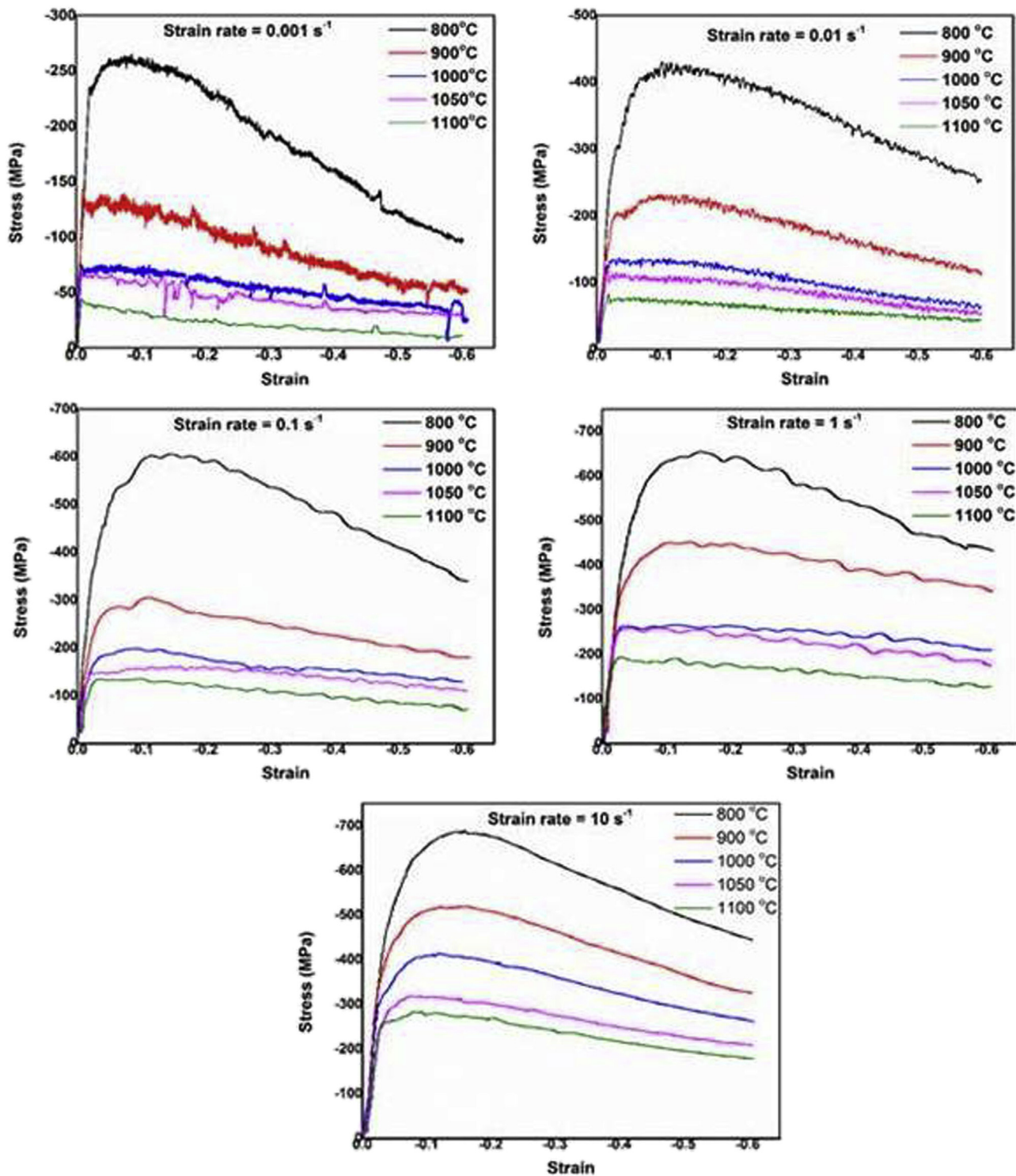


Fig. 3. True stress vs strain plot of as-cast AlCoCrFeNi_{2.1} EHEA at strain rate of 0.001, 0.01, 0.1, 1 and 10.

For an ideal linear power dissipater, $m = 1$ and $J_{\max} = \sigma \dot{\varepsilon}/2$. For a non-linear power dissipater, the efficiency of power dissipation is given by the following equation:

$$\eta = \frac{J}{J_{\max}} = \frac{2m}{m+1} \quad (7)$$

where m is the strain rate sensitivity parameter. This is an

important material property which can affect hot workability of material.

The variation of power efficiency (η) with strain rate ($\dot{\varepsilon}$) and temperature (T) constitutes the power dissipation map, which represents the power dissipation by the material through different metallurgical processes such as dynamic recovery, dynamic recrystallization, superplasticity etc. The condition for instability [21] can be defined:

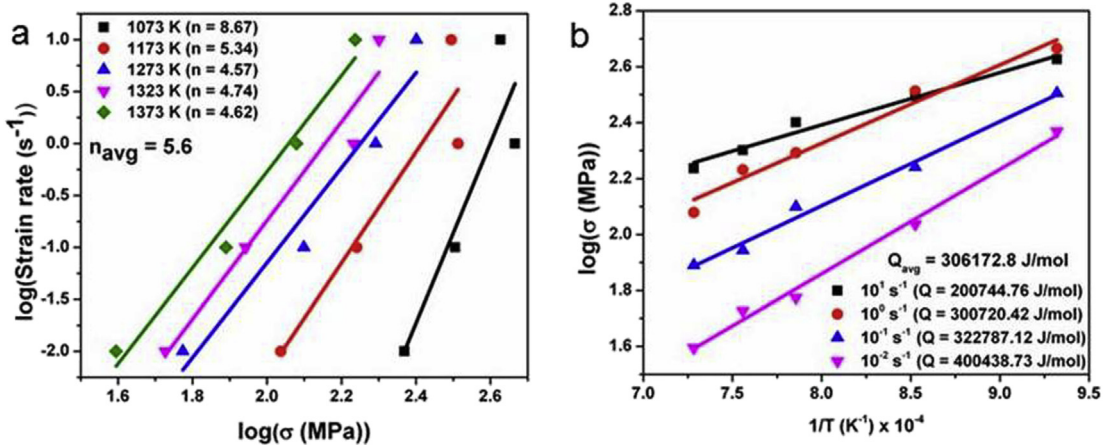


Fig. 4. (a) Plot between $\dot{\varepsilon}$ and σ and (b) σ and $1/T$; used for calculating the activation energy (Q).

$$\xi(\dot{\varepsilon}) = \left[\frac{\partial \ln(m/m+1)}{\partial \ln \dot{\varepsilon}} \right] + m \leq 0 \quad (8)$$

where $\xi(\dot{\varepsilon})$ is a dimensionless instability parameter and m is the strain rate sensitivity parameter. It has been reported [26] that the instability criterion (i.e. $2m < \eta \leq 0$) and stability condition (i.e. $0 < \eta \leq 2m$) during hot deformation are valid for any type stress-strain curve. The instability parameter, $\xi(\dot{\varepsilon})$ describes the flow behaviour of the material changes with the strain rate ($\dot{\varepsilon}$) and temperature (T) and hence constitute the instability map, delineating unstable and stable hot working conditions in the deformation processing map. Besides, the DMM also recommends the following criteria for stable plastic flow, i.e., the material flow is homogeneous during deformation,

$$0 < m < 1 \quad (9)$$

$$\dot{m} < 0 \quad (10)$$

$$s \geq 1 \quad (11)$$

$$\dot{s} = < 0 \quad (12)$$

where σ = flow stress, T = temperature in K, $\dot{\varepsilon}$ = strain rate, $\dot{m} = \frac{\delta m}{\delta \log \dot{\varepsilon}}$

$$s = \frac{\delta \ln \sigma}{\delta (\frac{1}{T})} \text{ and } \dot{s} = \frac{\delta s}{\delta \log \dot{\varepsilon}}$$

The variation of the instability parameters such as \dot{m} , \dot{s} and $\xi(\dot{\varepsilon})$ as a function of temperature and strain rate constitute the instability maps. These maps provide regions of stable plastic flow or homogeneous deformation and the unstable flow or inhomogeneous deformation [27,28]. The unstable plastic flow or inhomogeneous flow of materials often results in formation of cracks and leading to fracture of materials during deformation. From the point of view of forming of materials and during the service as stressed member, these regions of unstable plastic flow or inhomogeneous flow of materials should be avoided to restrict the failure of material.

Figs. 5 and 6 shows the isoefficiency contour and instability maps generated, the DMM stability parameters such as strain rate sensitivity of the flow stress (m), rate of change of strain rate

sensitivity with respect to strain rate (\dot{m}), temperature sensitivity of flow stress (s) and rate of change of temperature sensitivity of flow stress with respect to strain rate (\dot{s}) at true strains of $\epsilon = 0.05$ and 0.60 respectively; implying the different deformation mechanism at various combinations of temperatures and strain rates. The instability is generally characterized by the presence of cracks, localized plastic flow or adiabatic shear banding in the microstructure. Macroscopically, excessive bulging is also observed during the deformation under compressive loading conditions, diffuse necking in tensile loading and non-uniformity in axial and radial strain in the case of torsional loading and these are related to the geometry of the test samples. It has also been observed that these DMM stability parameters are unable to predict these geometries related instabilities [29] and the phenomenological criterion i.e. the flow localization parameter proposed by Semiatin and Jonas [30,31] predicts well about these geometries related instabilities. It is observed that the present studied EHEA is stable at high value of true strains for various combinations of deformation temperatures and strain rates. Fig. 5 (a) and 6 (a) reveal that at the stain of 0.05 the process efficiency is about 30% at 1200 K and at the strain rate of 10^{-2} s^{-1} and the efficiency increases with the increase in strain. In the regions where the process efficiency is higher (more than 30%) the microstructure of the deformed samples is free from any cracks. The instability regions predicted by $\xi(\dot{\varepsilon})$ are marked as shaded regions in Fig. 5 (a) and 6 (a). At stain of 0.05 there are two regions of instabilities i.e. one in the temperature range 1073 K to 1200 K at strain rate above 10^{-2} s^{-1} and the other is in the temperature range 1300 K to 1373 K at strain rate above 1 s^{-1} . As strain increases to 0.6 these instability regions widened and merged. In general, the instability occurs at strain rates above 1 s^{-1} as indicated in Fig. 6 (a). The parameter m predicts that there is no instability in the investigated temperature and strain rate regimes and there is no change in predictions with the increase in strain. The stability regions predicted by the other two parameters \dot{m} and s are indicated in Figs. 5 (c) and 6 (c) & 5 (d) and 6 (d) respectively as hatched areas. These two parameters predict only narrow regions of instability and the effect of stain on the prediction of instability regions is small. The stability regions predicted by the parameter \dot{s} at strain levels of 0.05 and 0.6 are indicated in Fig. 5 (e) and Fig. 6 (e) respectively as hatched areas. The prediction by the parameter \dot{s} is strongly dependent on strain and the flow is tending to stable as strain increases. The predictions are in general coinciding with the predictions of processing efficiency parameter, $\xi(\dot{\varepsilon})$ (Figs. 5 (a) and 6 (a)). It is to be noted that the parameters, $\xi(\dot{\varepsilon})$ and \dot{s} are functions of both temperature and strain rate and taking care of synergistic

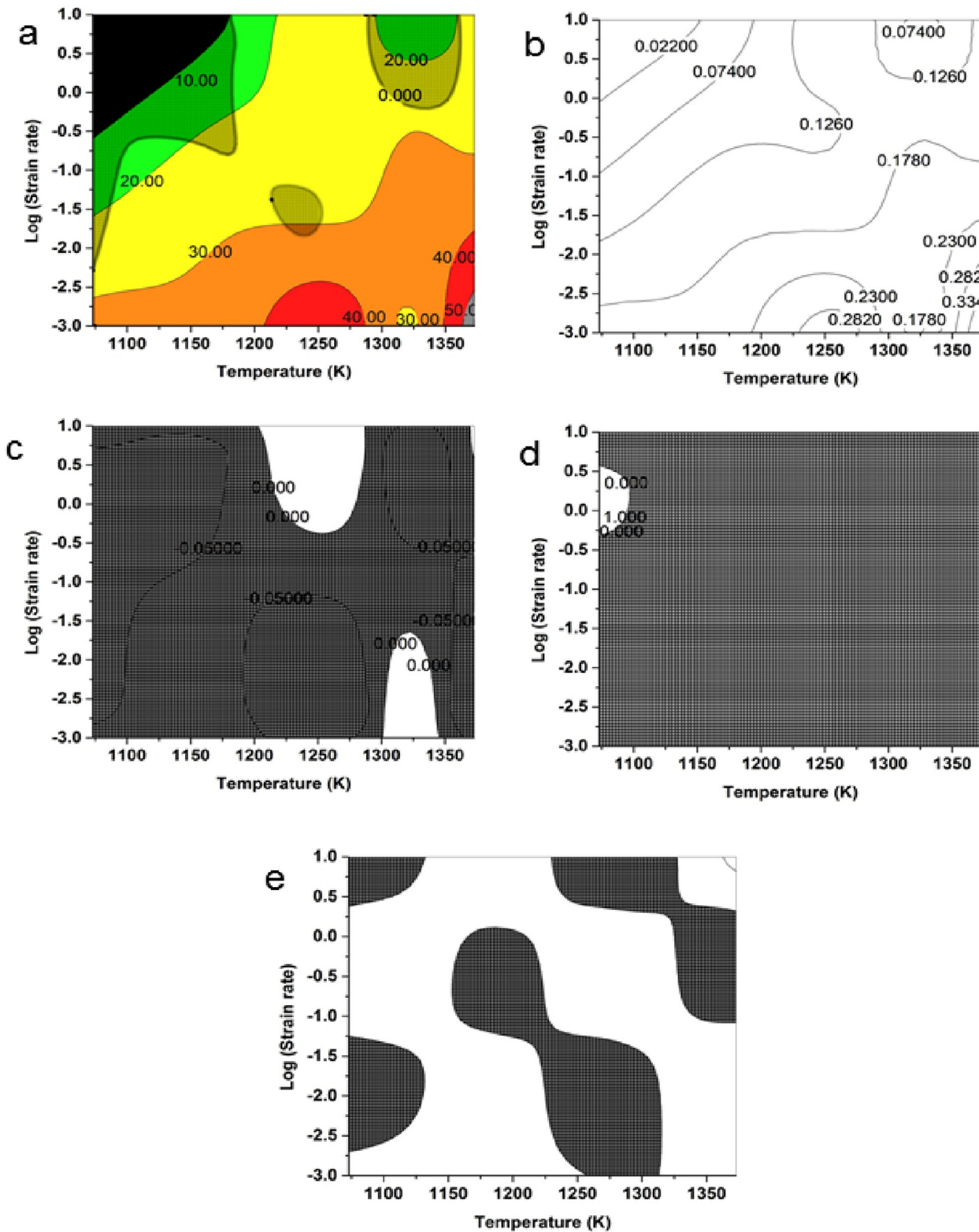


Fig. 5. (a) Processing map at 0.05 strain, (b) Strain rate sensitivity, (c) \ln , (d) s and (e) \bar{s}

effects of temperature, strain and strain rate. To summarize our observation using DMM processing and instability maps, it has been observed that the material exhibits stable plastic flow in the temperature range 1073–1150 K and 10^{-3} – $10^{-2.2}$ s $^{-1}$ as well as 1338–1373 K and 10^{-3} – $10^{-1.2}$ s $^{-1}$, that are normally envisaged for

engineering applications at high temperatures.

6. Microstructural analysis of the deformed samples

The microstructural characterization of the investigated

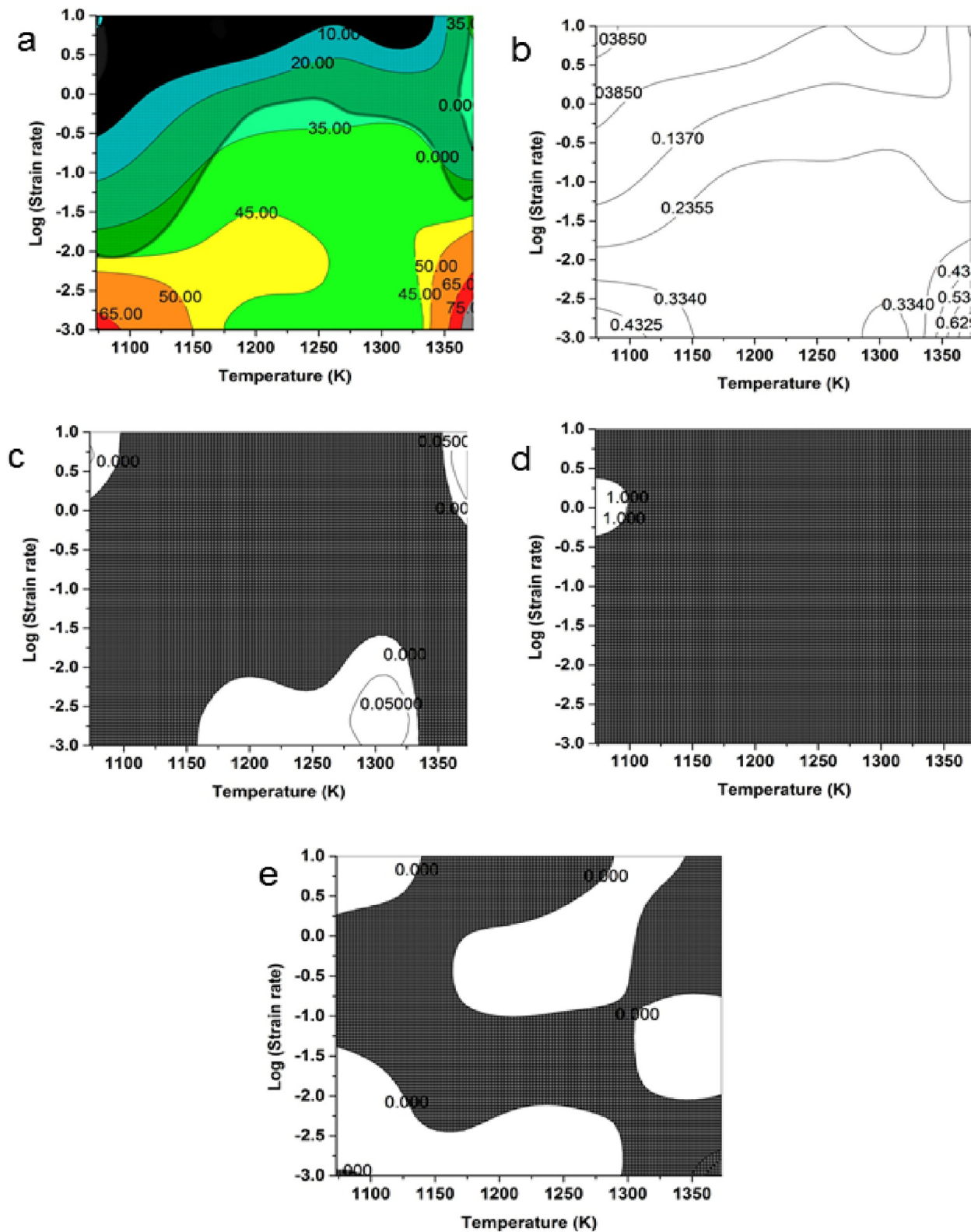


Fig. 6. (a) Processing map at 0.6 strain, (b) Strain rate sensitivity, (c) \dot{m} , (d) s and (e) \dot{s}

deformed EHEA at different strain rates and temperatures was carried out to correlate with the observations drawn from the deformation processing maps. The microstructure of deformed

sample at last stage of deformation at different combination of strain rates and temperatures is shown in Fig. 7 and correlated with different regimes in deformation processing maps. The detailed

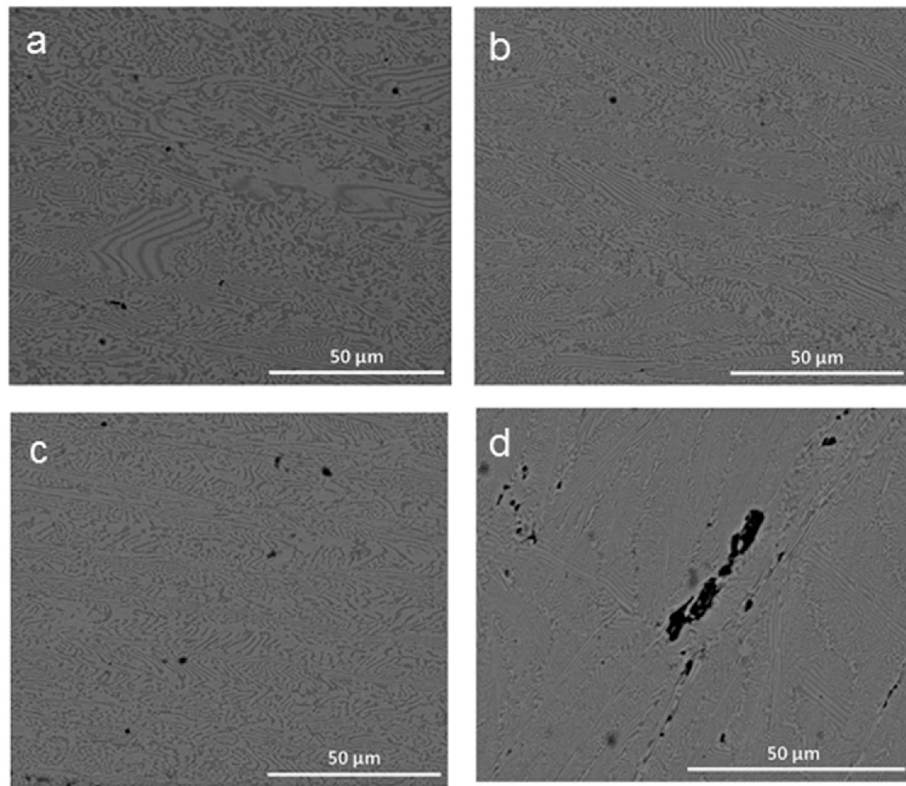


Fig. 7. Shows SEM BSE images of deformed sample at (a) 0.001 @800 °C, (b) 0.001@ 900° C, (c) 0.001@1000 °C and (d) 10@1000 °C.

microstructural analysis of the deformed specimens indicates uniform distribution in the stable regime, whereas adiabatic shear banding or localized plastic flow, pores etc. in the microstructure are characteristics of the deformed specimen in the unstable regime. It is also to be noted that the macroscopic cracks are observed at the centre of the sample regions at above 1050 °C and

lower strain rate of 0.001 which may be attributed to the dead metal zone meeting. [Fig. 1S](#) (Refer to Supplementary file) shows the effective stress variation with respect to stroke at four different positions (1, 2, 3, and 4). Point 1 is at centre of the sample and other points are away from the centre and point 4 at the surface. It is clear from the plot that at the centre position the stress was increasing

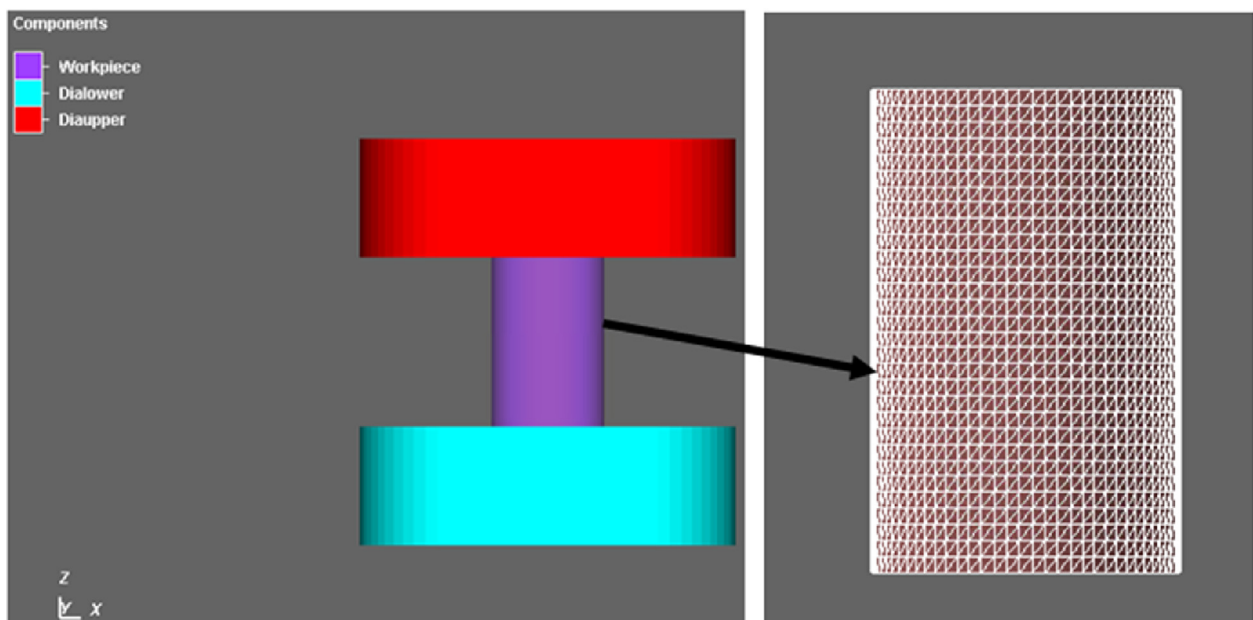


Fig. 8. The geometry for FEM simulation.

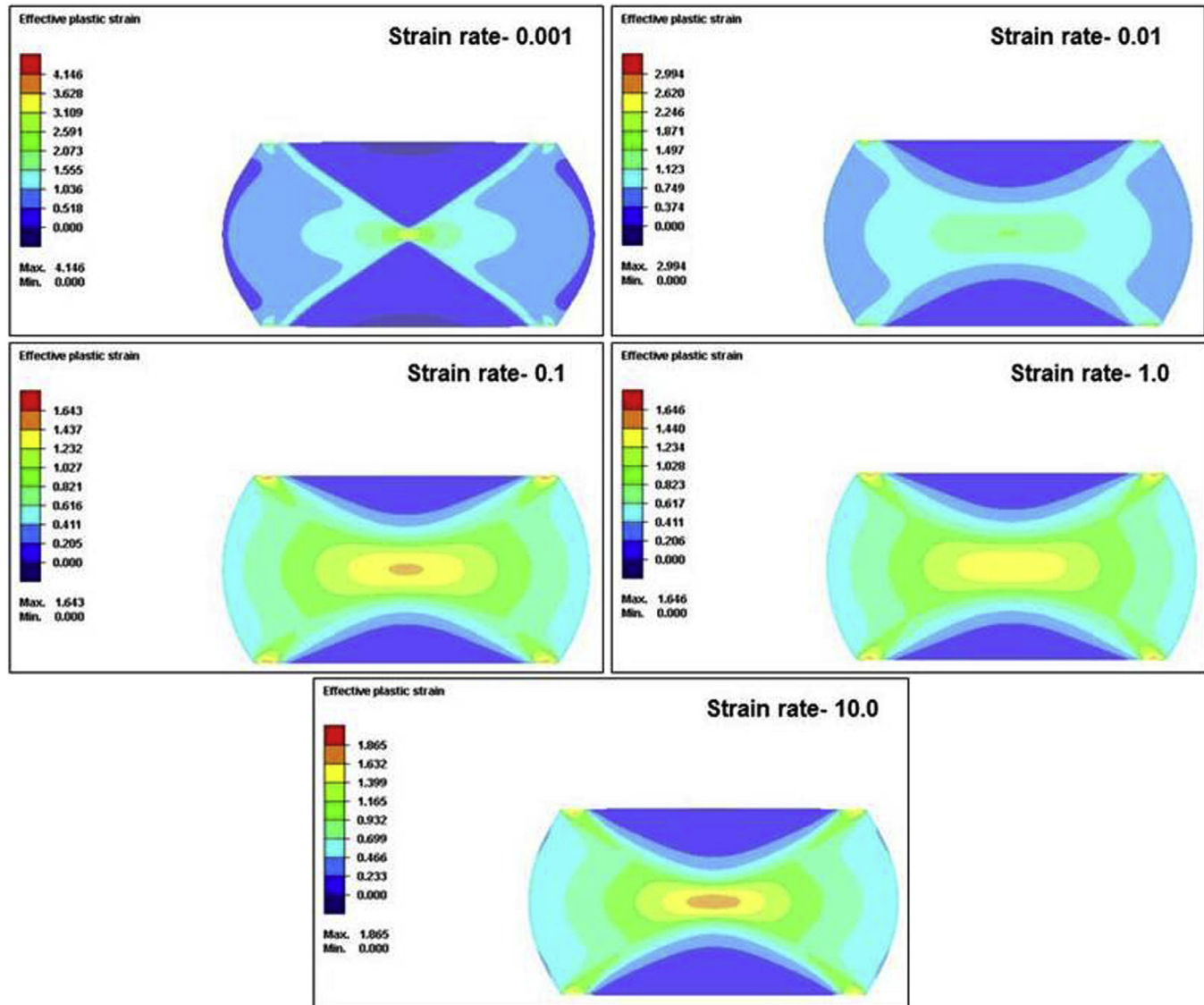


Fig. 9. Simulated plastic strain field distribution at different strain rate at 1000 °C.

after a particular amount of stroke movement, this is attributed to the dead metal zones meeting at centre. It is to be noted that the macroscopic crack at the high efficiency regimes ($>1323\text{ K}$) is attributed to the geometrical reason rather than metallurgical effects. Therefore, multicomponent EHEAs consisting of both solid solution phase and intermetallic compound in the eutectics can be considered as potential candidates for high temperature structural applications.

7. FEM simulation

Hot deformation process was simulated using FEM simulation package at different temperatures and strain rates condition. The geometry for FEM simulation is given in Fig. 8. The experimental stress-strain data obtained from Gleeble 3800® thermo-mechanical simulator at different combination of deformation temperatures and strain rates was used to simulate the hot compression process. The contour map (shown in Fig. 9) indicates the strain field distribution of sample after 50% deformation. It is clear that the strain

field within the sample varies according to the stain rate as well as temperature. In all cases, the material is highly strained at the centre and the flowability was less near contact area due to friction as expected. The inhomogeneity within the sample can be clearly verified with the help of FEM simulations. The material characterization for the correlation of processing map is carried out by considering the strain field distribution obtained from FEM simulation. Effective strain field shows largest strain occurring at low strain rate condition at the centre of the sample.

Fig. 10 (a) shows the material flow vectors during compression of sample at strain rate 10 s^{-1} and at 1000 °C (axisymmetric section was taken). Here the upper die is moving and lower die is stationary analogous to left and right rams of hydrawedge® module in Gleeble®. The material flow vectors show high magnitude at the moving die side and lower magnitude at the stationary side. From the flow pattern, it is observed that the flow of material occurs in the perpendicular direction of ram movement which is one the factors for barreling. The material flow behaviour can be used to predict the final shape of the formed material. Fig. 10 (b) shows the

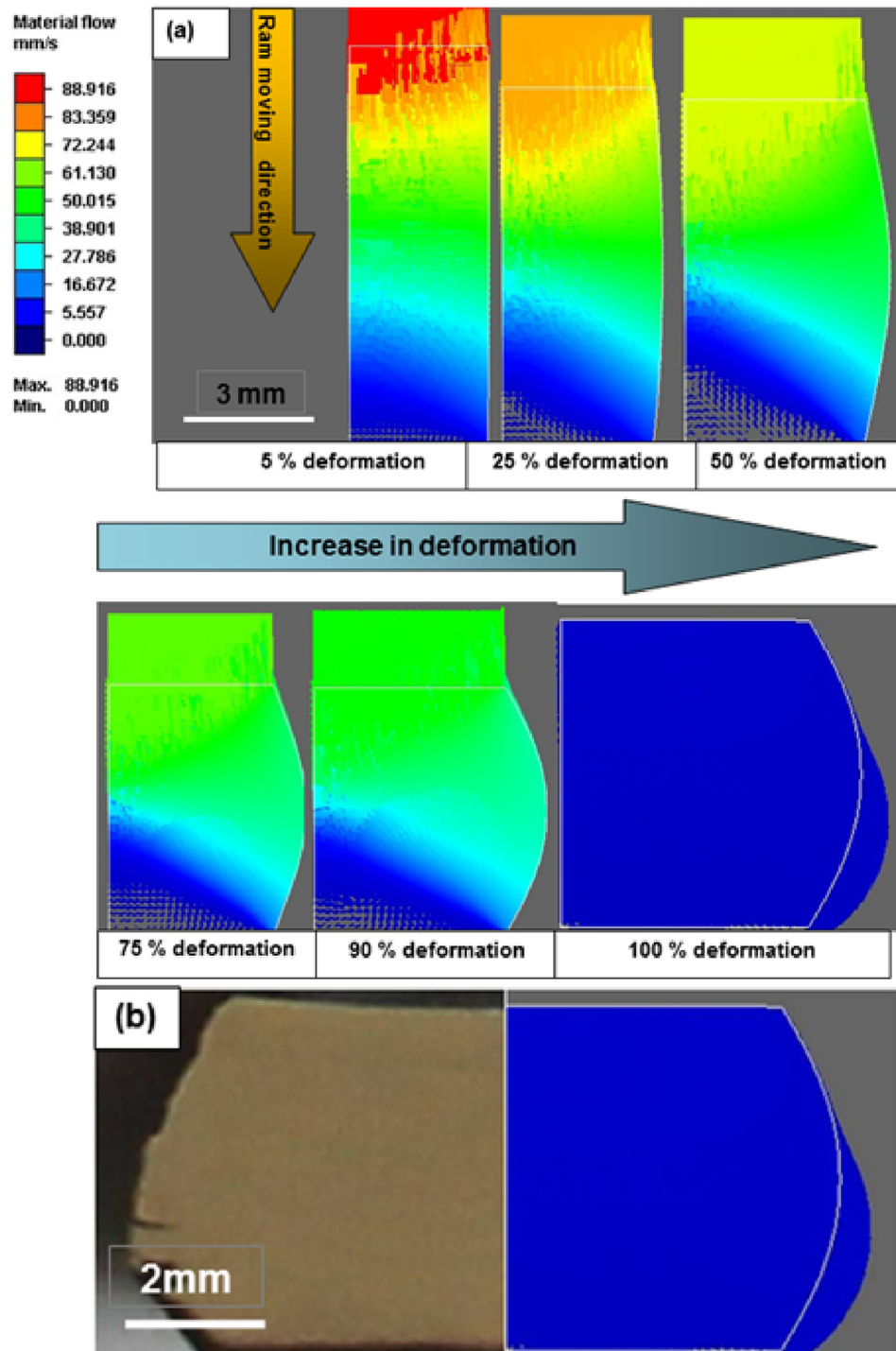


Fig. 10. (a) Material flow behaviour during high temperature compression (10 strain rate@1000 °C), (b) Comparison of geometry after compression for 10 strain rate@1000 °C.

comparison of actual sample (central cross section) compressed at strain rate 10 s^{-1} and at 1000 °C after deformation. Fig. 11 shows the comparison of true stress vs. stroke behaviour at strain rate 10 s^{-1} and at 1000 °C at point in the deformed sample. It is found that the simulated true stress vs. stroke curve differs from the corresponding experimental curve which may be due the effect of barreling. The difference between experimental and simulated results is minimized by modifying the material model parameters so that

the regression coefficient (R^2) between simulated true stress vs. stroke curve and corresponding experimental curve is greater than 0.99. The micro-hardness distribution at strain rate 10 s^{-1} and 1000 °C is shown in Fig. 12, which confirms the strain field distribution pattern inside the sample. Minor deviations in microhardness data from the expected trend could be attributed to the possible effect of dead metal zone. By a combination of thermo-mechanical simulation, deformation instability analysis and FEM

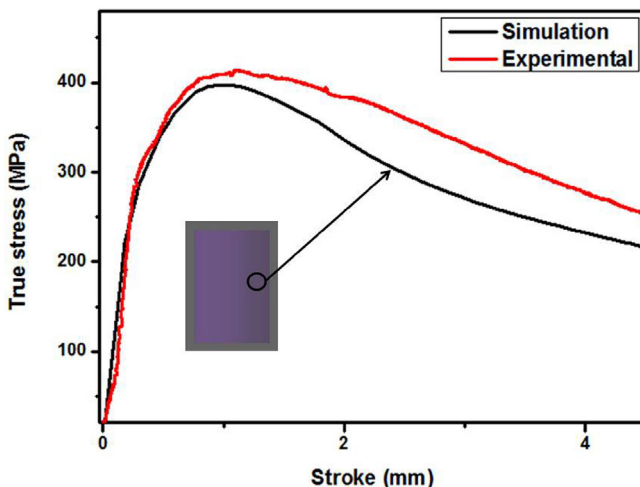


Fig. 11. Comparison of stroke vs. true stress (10 strain rate @1000 °C).

simulations, this study thus opens an integrated approach to obtain stable microstructures in a final component of emerging high entropy alloys through high temperature deformation.

8. Conclusions

The hot working characteristics of the multicomponent AlCoCrFeNi_{2.1} EHEA have been investigated through compressive tests in the temperature range 800–1100 °C with the strain rate varying from 10^{-3} – 10^1 s⁻¹. The following conclusions can be drawn based upon the results obtained in the investigated multicomponent EHEA:

The average activation energy calculated using power law equation is ~306 kJ/mol and stress exponent value is ~5.6.

The optimum thermo-mechanical window is 1073–1150 K and strain rate 10^{-3} – $10^{-2.2}$ s⁻¹ as well as in the range 1338–1373 K and 10^{-3} – $10^{-1.2}$ s⁻¹.

FEM model coupled with thermomechanical simulation using Gleeble® establishes the strain field distribution and material flow pattern at different conditions.

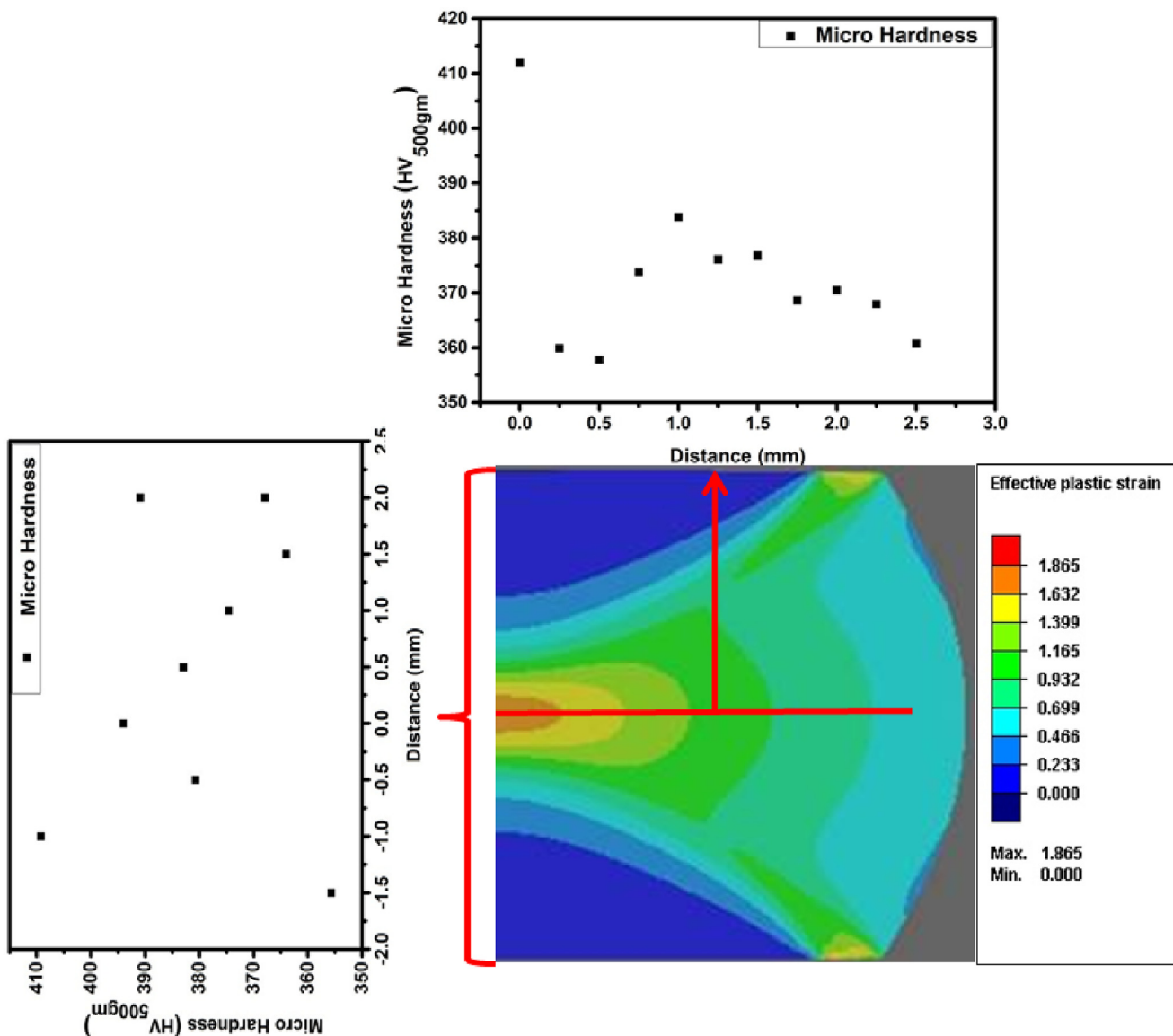


Fig. 12. Variation of micro-hardness within the sample (1000 °C @10 strain rate).

Appendix A. Supplementary data

Supplementary data related to this article can be found at <https://doi.org/10.1016/j.jallcom.2018.03.262>.

References

- [1] J.W. Yeh, S.K. Chen, S.J. Lin, J.Y. Gan, T.S. Chin, T.T. Shun, et al., Nanostructured high-entropy alloys with multiple principal elements: novel alloy design concepts and outcomes, *Adv. Eng. Mater.* 6 (2004), <https://doi.org/10.1002/adem.200300567>, 299–303+274.
- [2] B. Cantor, I.T.H. Chang, P. Knight, a. J.B. Vincent, Microstructural development in equiatomic multicomponent alloys, *Mater. Sci. Eng. A* 375–377 (2004) 213–218, <https://doi.org/10.1016/j.msea.2003.10.257>.
- [3] S. Praveen, B.S. Murty, R.S. Kottada, Alloying behavior in multi-component AlCoCrCuFe and NiCoCrCuFe high entropy alloys, *Mater. Sci. Eng. A* 534 (2012) 83–89, <https://doi.org/10.1016/j.msea.2011.11.044>.
- [4] J.-W. Yeh, S.-J. Lin, T.-S. Chin, J.-Y. Gan, S.-K. Chen, T.-T. Shun, et al., Formation of simple crystal structures in Cu-Co-Ni-Cr-Al-Fe-Ti-V alloys with multi-principal metallic elements, *Metall. Mater. Trans. A* 35 (2004) 2533–2536, <https://doi.org/10.1007/s11661-006-0234-4>.
- [5] S. Guo, C. Ng, C.T. Liu, Sunflower-like solidification microstructure in a near-eutectic high-entropy alloy, *Mater. Res. Lett.* 1 (2013) 228–232, <https://doi.org/10.1080/21663831.2013.844737>.
- [6] S. Mridha, S. Samal, P.Y. Khan, K. Biswas, Govind, Processing and consolidation of nanocrystalline Cu-Zn-Ti-Fe-Cr high-entropy alloys via mechanical alloying, *Metall. Mater. Trans. A Phys. Metall. Mater. Sci.* 44 (2013) 4532–4541, <https://doi.org/10.1007/s11661-013-1824-6>.
- [7] A.K. Mishra, S. Samal, K. Biswas, Solidification behaviour of Ti-Cu-Fe-Co-Ni high entropy alloys, *Trans. Indian Inst. Met.* 65 (2012) 725–730, <https://doi.org/10.1007/s12666-012-0206-x>.
- [8] S. Samal, S. Mohanty, A.K. Misra, K. Biswas, B. Govind, Mechanical behavior of novel suction cast Ti-Cu-Fe-Co-Ni high entropy alloys, *Mater. Sci. Forum* 790–791 (2014) 503–508, <https://doi.org/10.4028/www.scientific.net/MSF.790-791.503>.
- [9] B.S. Murty, J.W. Yeh, S. Ranganthan, *High Entropy Alloys*, Elsevier, 2014.
- [10] Y. Zhang, T. Ting, Z. Tang, M.C. Gao, K.A. Dahmen, P.K. Liaw, et al., Progress in materials science microstructures and properties of high-entropy alloys, *Prog. Mater. Sci.* 61 (2014) 1–93, <https://doi.org/10.1016/j.pmatsci.2013.10.001>.
- [11] K. Tsai, M. Tsai, J. Yeh, Sluggish diffusion in Co – Cr – Fe – Mn – Ni high-entropy alloys, *Acta Mater.* 61 (2013) 4887–4897, <https://doi.org/10.1016/j.actamat.2013.04.058>.
- [12] D.L. Beke, G. Erdélyi, On the diffusion in high-entropy alloys, *Mater. Lett.* 164 (2016) 111–113, <https://doi.org/10.1016/j.matlet.2015.09.028>.
- [13] O.N. Senkov, G.B. Wilks, J.M. Scott, D.B. Miracle, Mechanical properties of Nb 25Mo 25Ta 25W 25 and V 20Nb 20Mo 20Ta 20W 20 refractory high entropy alloys, *Intermetallics* 19 (2011) 698–706, <https://doi.org/10.1016/j.intermet.2011.01.004>.
- [14] S. Mohanty, S. Samal, a. Tazuddin, C.S. Tiwary, N.P. Gurao, K. Biswas, Effect of processing route on phase stability in equiatomic multicomponent Ti 20 Fe 20 Ni 20 Co 20 Cu 20 high entropy alloy, *Mater. Sci. Technol.* 31 (2015) 1214–1222, <https://doi.org/10.1179/1743284715Y.0000000024>.
- [15] I.S. Wani, T. Bhattacharjee, S. Sheikh, Y.P. Lu, S. Chatterjee, P.P. Bhattacharjee, et al., Ultrafine-grained AlCoCrFeNi_{2.1} eutectic high-entropy alloy, *Mater. Res. Lett.* 4 (2016) 174–179, <https://doi.org/10.1080/21663831.2016.1160451>.
- [16] S. Samal, M.R. Rahul, R.S. Kottada, G. Phanikumar, Hot deformation behaviour and processing map of Co-Cu-Fe-Ni-Ti eutectic high entropy alloy, *Mater. Sci. Eng. A* 664 (2016) 227–235, <https://doi.org/10.1016/j.res.2015.11.012>.
- [17] Y. Lu, Y. Dong, S. Guo, L. Jiang, H. Kang, T. Wang, et al., A promising new class of high-temperature alloys: eutectic high-entropy alloys, *Sci. Rep.* 4 (2014) 1–5, <https://doi.org/10.1038/srep06200>.
- [18] H. Jiang, K. Han, X. Gao, Y. Lu, Z. Cao, M.C. Gao, et al., A new strategy to design eutectic high-entropy alloys using simple mixture method, *Mater. Des.* 142 (2018) 101–105, <https://doi.org/10.1016/j.matedes.2018.01.025>.
- [19] L. Jiang, Z.Q. Cao, J.C. Jie, J.J. Zhang, Y.P. Lu, T.M. Wang, T.J. Li, Effect of Mo and Ni elements on microstructure evolution and mechanical properties of the CoFeNi_xM_y high entropy alloys, *J. Alloys Compd.* 649 (2015) 585–590.
- [20] H. Jiang, L. Jiang, D. Qiao, Y. Lu, T. Wang, Z. Cao, et al., Effect of niobium addition on microstructure and properties of the CoCrFeNb_xNi high entropy alloys, *J. Mater. Sci. Technol.* 33 (2016) 712–717, <https://doi.org/10.1016/j.jmst.2016.09.016>.
- [21] Y. Dong, Y. Lu, J. Kong, J. Zhang, T. Li, Microstructure and mechanical properties of multi-component AlCrFeNi_xMo_y high-entropy alloys, *J. Alloys Compd.* 573 (2013) 96–101.
- [22] Q.L. Dai, B.B. Sun, M.L. Sui, G. He, Y. Li, J. Eckert, et al., High-performance bulk Ti-Cu-Ni-Sn-Ta nanocomposites based on a dendrite-eutectic microstructure, *J. Mater. Res.* 19 (2011) 2557–2566, <https://doi.org/10.1557/JMR.2004.0332>.
- [23] S. Roy, S. Suwas, The influence of temperature and strain rate on the deformation response and microstructural evolution during hot compression of a titanium alloy Ti-6Al-4V-0.1B, *J. Alloys Compd.* 548 (2013) 110–125, <https://doi.org/10.1016/j.jallcom.2012.08.123>.
- [24] Y.V.R.K. Prasad, H.L. Gege, S.M. Doraivelu, J.C. Malas, J.T. Morgan, K.A. Lark, D.R. Barker, Modeling of dynamic material behavior in hot deformation: forging of Ti-6242, *Metall. Trans. A* 15 (1984) 1883–1892.
- [25] H.L. Gege, J.C. Malas, S.M. Doraivelu, V.A. Shinde, *Metals Hand Book*, vol. 14, ASM International, Materials Park, OH, 1987.
- [26] Y.V.R.K. Prasad, K.P. Rao, S. Sasidara, *Hot Working Guide: a Compendium of Processing Maps*, ASM International, Metals Park, OH, 2015.
- [27] J.C. Malas, Venkat Seetharaman, Using material behavior models to develop process control strategies, *J. Miner. Met. Mater. Soc.* 44 (1992) 8–13.
- [28] S. Venugopal, S.L. Mannan, Y.V.R.K. Prasad, Criteria for prediction of flow in stabilities and microstructural manifestations during warm working of AISI 304L stainless steel, *Mater. Sci. Technol.* 9 (1993) 1021–1030.
- [29] S. Venugopal, S.L. Mannan, Y.V.R.K. Prasad, Processing map for mechanical working of stainless steel, *Scr. Metall. Mater.* 28 (1995) 715–720.
- [30] S.L. Semiatin, G.D. Lahotti, Deformation and unstable flow in hot forging of Ti-6Al-2Sn-4Zr-2Mo-0.1Si, *Metall. Mater. Trans. A* 12 (1981) 1705–1717.
- [31] S.L. Semiatin, J.J. Jonas, *Formability and Workability of Metals: Plastic Instability and Flow Localisation*, ASM, Metals Park, OH, 1984.